small methods
www.small-methods.com

Covalently Functionalized MXenes for Highly Sensitive Humidity Sensors

Iwona Janica, Verónica Montes-García, Francesca Urban, Payam Hashemi, Ali Shaygan Nia, Xinliang Feng, Paolo Samorì, and Artur Ciesielski**

Transition metal carbides and nitrides (MXenes) are an emerging class of 2D materials, which are attracting ever-growing attention due to their remarkable physicochemical properties. The presence of various surface functional groups on MXenes' surface, e.g., –F, –O, –OH, –Cl, opens the possibility to tune their properties through chemical functionalization approaches. However, only a few methods have been explored for the covalent functionalization of MXenes and include diazonium salt grafting and silylation reactions. Here, an unprecedented two-step functionalization of $Ti_3C_2T_x$ MXenes is reported, where (3-aminopropyl)triethoxysilane is covalently tethered to $Ti_3C_2T_x$ and serves as an anchoring unit for subsequent attachment of various organic bromides via the formation of C–N bonds. Thin films of $Ti_3C_2T_x$ functionalized with linear chains possessing increased hydrophilicity are employed for the fabrication of chemiresistive humidity sensors. The devices exhibit a broad operation range (0–100% relative humidity), high sensitivity (0.777 or 3.035), a fast response/recovery time (0.24/0.40 s ΔH^{-1}, respectively), and high selectivity to water in the presence of saturated vapors of organic compounds. Importantly, our $Ti_3C_2T_x$-based sensors display the largest operating range and a sensitivity beyond the state of the art of MXenes-based humidity sensors. Such outstanding performance makes the sensors suitable for real-time monitoring applications.

1. Introduction

Humidity sensors have become indispensable for many applications including agriculture,[1–2] medicine,[3] or food industry[4] as well as for our living comfort.[5] The fields of applications are fast expanding, together with a gigantic demand for devices capable of monitoring and controlling the relative humidity (RH) level in very specific conditions (i.e., certain operation range, sensitivity, response/recovery time, environment, etc.). The current market-dominating sensing elements include ceramics,[6] metal oxides,[7] and conducting polymers[6,8] which exhibit some unavoidable drawbacks, such as long response and recovery times, low sensitivity, high hysteresis, and low long-term stability. Therefore, the development of smaller, more reliable, and better-performing humidity sensors is highly sought-after.

Two-dimensional materials (2DMs)[9–11] have emerged during the last decade as the ideal components

I. Janica
Faculty of Chemistry
Adam Mickiewicz University in Poznań
Uniwersytetu Poznańskiego 8, Poznań 61-614, Poland

I. Janica, A. Ciesielski
Centre for Advanced Technologies
Adam Mickiewicz University in Poznań
Uniwersytetu Poznańskiego 10, Poznań 61-614, Poland
E-mail: ciesielski@unistra.fr

I. Janica, V. Montes-García, F. Urban, P. Samorì, A. Ciesielski
Université de Strasbourg
CNRS
ISIS
8 allée Gaspard Monge, Strasbourg 67000, France
E-mail: samori@unistra.fr

P. Hashemi, A. S. Nia, X. Feng
Center for Advancing Electronics Dresden and Faculty of Chemistry and Food Chemistry
Technische Universität Dresden
Mommsenstrasse 4, 01062 Dresden, Germany

P. Hashemi, A. S. Nia, X. Feng
Max Planck Institute for Microstructure Physics
Weinberg 2, 06120 Halle, Germany

The ORCID identification number(s) for the author(s) of this article can be found under https://doi.org/10.1002/smtd.202201651

DOI: 10.1002/smtd.202201651

for the next generation of highly efficient humidity sensors due to their high surface area-to-volume ratios, ultrahigh surface sensitivity to the environment, and superior optoelectronic properties combined with their excellent mechanical characteristics, such as robustness and flexibility.[12–14] Among the plethora of available 2DMs, graphene oxide (GO)[15] and reduced graphene oxide (rGO)[16] are the most extensively studied materials due to their large-scale and straightforward production, relatively low cost of starting materials, and chemical stability.[13] The presence of various oxygen-containing groups, such as epoxy, hydroxyl, and carbonyl groups, on the basal plane and edges of GO, endows it with a hydrophilic character, enhancing its interaction with water.[17] For instance, an impedimetric humidity sensor based on solely GO as sensing material displayed an unprecedented response speed (≈30 ms response and recovery times).[15] However, due to its low conductivity,[18] either electrochemical impedance spectroscopy (EIS) needs to be used as a readout, which is not suitable for practical applications, or high potentials need to be applied in order to reach readable currents, hence increasing the power consumption.[19] In addition, at high RH levels, GO usually displays large hysteresis and poor stability/reusability.[17] Contrary, rGO exhibits significantly higher conductivity and stability than GO,[20–21] but due to the reduced amount of oxygen functional groups, it has a hydrophobic nature, leading to a lower responsivity to humidity.[13,22]

Recently, MXenes, early transition metals carbides and/or nitrides, with the general formula $M_{n+1}XT_x$ (M – an early transition metal, X is C and/or N, T_x – surface-terminating functional groups, e.g. –F, –O, –OH, –Cl, etc.)[23] are attracting great attention in various fields of research. MXenes provide solutions for the drawbacks of GO and rGO as they possess a hydrophilic nature due to the presence of oxygen-containing groups on their surface as well as high electrical conductivity (≈15 000 S cm^{-1}) that enables the fabrication of low-power devices. In only one decade, over 30 different MXenes have been already prepared, such as $Ti_3C_2T_x$,[24] V_2CT_x,[25] Nb_2CT_x,[26] $Zr_3C_2T_x$,[27] Mo_2CT_x,[28] or $(Mo_2Ti_2)C_3T_x$.[29] Although this family of materials is still in its infancy, its high potential has been already demonstrated in few applications such as in energy storage,[30–33] catalysis,[34–37] and chemical sensing of various gases, such as NO_2 or CO_2,[38–40] biological compounds, e.g., dopamine or urea,[41–42] as well as strain or pressure sensors.[11,43–44]

Since the first MXene-based humidity sensor demonstration in 2017,[45] different strategies have been explored to boost the performance of MXene as active material in sensors. Ion intercalation[45] (e.g., K^+, Mg^{2+}, or Na^+) in the pristine MXenes structures has been used to promote the diffusion of water in the material, improving its sensitivity toward moisture. Hybridization with Ag nanowires,[46] titanium dioxide (TiO_2),[47] $K_2Ti_4O_9$ nanowires,[48] and water-sensitive polyelectrolytes such as poly(vinyl alcohol) (PVA),[49] poly(dopamine) (PDA),[50] or poly(diallyldimethylammonium chloride) (PDAC)[51] has been employed to increase the responsiveness (i.e., response and recovery time) of pristine MXenes. The intercalation of $TiOF_2$ nanospheres[52] in the pristine MXenes, or their hybridization with sodium ascorbate[53] or sodium alginate[54] showed improved long-term stability. Noteworthy, the interaction of MXenes with water usually leads to the formation of TiO_2 and the loss of the high electrical conductivity of MXenes,[55] leading to poor reusability/cyclability. Finally, pristine MXenes show poor selectivity for water, as $Ti_3C_2T_x$ has proved being sensitive to rather low concentrations of ketones (< to 50 ppb),[56–57] alcohols (< to 100 ppb),[58] and ammonia (< to 100 ppb)[59] vapors at room temperature. Although some progress have been made, the overall performance of MXene-based humidity sensors still needs to be improved in terms of sensitivity, responsiveness, reusability, and selectivity for true practical applications.

Fortunately, all these problems can be overcome through the covalent functionalization of MXenes with small organic molecules exhibiting high affinity for water, which not only can increase the MXenes stability and boost their sensitivity via the increase of interlayer separation, but also guarantee a selective and fast interaction with moisture.[21] The main two strategies followed for the covalent functionalization of MXenes with small molecules rely on diazonium salts[60] and silylation reactions.[61] Although these approaches allow the tuning of MXene's stability and their electrical properties, a more versatile strategy is needed to provide MXenes with on-demand functionality.

Here, we report the synthesis of $Ti_3C_2T_x$ MXenes through a fluoride etching process and their covalent functionalization via a two-step reaction. First, (3-aminopropyl)triethoxysilane (APTES, F1) [28] is anchored via a silylation reaction and then a secondary modification is performed through the formation of a C–N covalent bond between F1 and small organic molecules chosen based on their very different affinity towards water molecules, i.e., 1-bromohexane (F2), 1-bromo-2-(2-methoxyethoxy)ethane (F3), or 6-bromo-1-hexanol (F4). Thin films of pristine and functionalized $Ti_3C_2T_x$ are then employed as active layers in chemiresistive humidity sensors. We evaluate the main key performance indicators (KPIs) of pristine and functionalized $Ti_3C_2T_x$ sensors in terms of operation range, sensitivity, response/recovery time, selectivity, and temperature dependence. X-ray diffraction analysis at different RH levels is performed to shed some light on the humidity sensing mechanism of functionalized $Ti_3C_2T_x$ sensors. As a proof of concept, we showcase the performance of our sensor in a practical application, as humidity sensors in smart diapers.

2. Results and Discussion

2.1. Preparation of Functionalized $Ti_3C_2T_x$

The schematic representation of the preparation of $Ti_3C_2T_x$ MXenes and their functionalization is presented in **Figure 1**. First, Ti_3AlC_2 MAX is etched using a mixture of hydrofluoric acid: deionized water: hydrochloric acid with the ratio 1:3:6 v/v first at 0°C for 60 min and then at 35°C for 24 h (see the Experimental Section for details). MXene particles are washed by successive steps of centrifugation and then exfoliated at 25°C for 24 h employing lithium chloride (LiCl) solution, which acts as an intercalating agent during sonication process, leading to $Ti_3C_2T_x$. Prior to functionalization $Ti_3C_2T_x$ MXenes are thoroughly purified via multiple centrifugation steps. Subsequently, amino-functionalized $Ti_3C_2T_x$ is prepared by the covalent functionalization of $Ti_3C_2T_x$ with (3-aminopropyl)triethoxysilane (APTES, F1) at room temperature for 2 days. $Ti_3C_2T_x$-F1 is obtained as a result of the covalent bond formation between the silanol groups of the silanol coupling agent, after the hydrolysis reaction, and the hydroxyl groups present on the surface of $Ti_3C_2T_x$. The

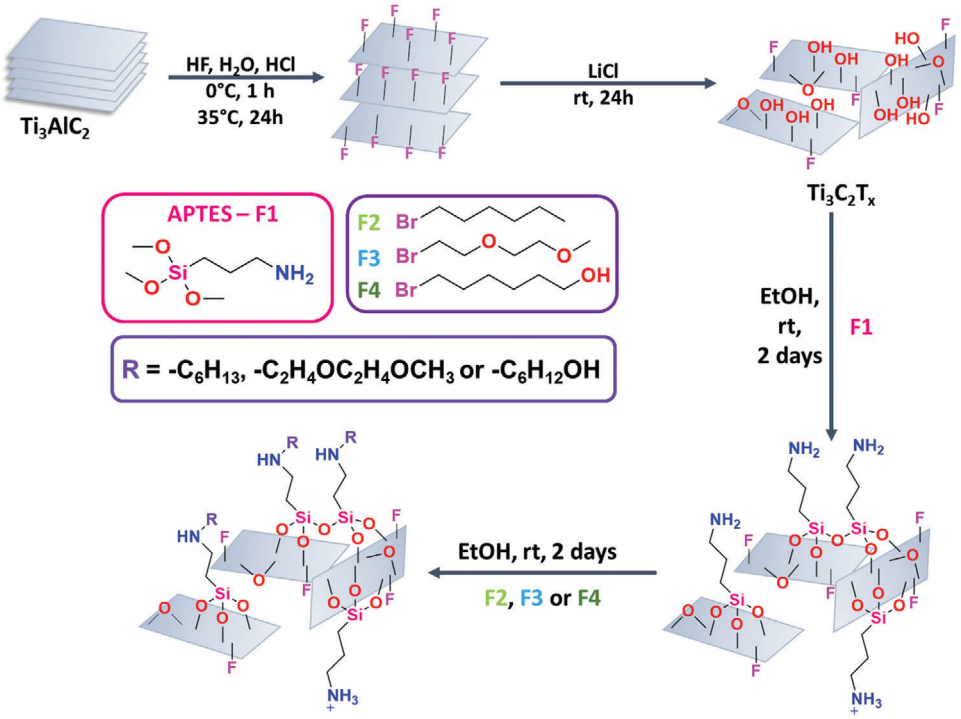

Figure 1. Schematic representation of the production of functionalized $Ti_3C_2T_x$.

second functionalization step with 1-bromohexane (F2), 1-bromo-2-(2-methoxyethoxy)ethane (F3), or 6-bromo-1-hexanol (F4) is then performed through the covalent C–N bond formation between F2, F3, or F4 and F1 at room temperature for 2 days. Finally, $Ti_3C_2T_x$-F1+F2, $Ti_3C_2T_x$-F1+F3, and $Ti_3C_2T_x$-F1+F4 are obtained. After the two-step functionalization, the concentration of the solutions in ethanol is ≈1.5 mg mL^{-1} in all cases. The optical images of MXene-based solutions before and after functionalization are presented in Figure S1 (Supporting Information).

The average zeta potential for the pristine MXene, $Ti_3C_2T_x$, is negative, −42.71 mV, due to the presence of numerous negative groups on the surface of $Ti_3C_2T_x$, such as F^- or OH^-.[62] After the functionalization with F1, the zeta potential value increases to +55.06 mV, while after subsequent modification with brominated compounds F2, F3, or F4, the value increases to +65.53, +76.63, and +75.52 mV, respectively, which provides the first indication of successful functionalization of $Ti_3C_2T_x$.

In order to gain insight into the material's composition changes, X-ray photoelectron spectroscopy (XPS) analysis is performed. After the initial functionalization of $Ti_3C_2T_x$ with F1, as can be seen in the survey spectra (Figure S2, Supporting Information), the intensity of oxygen, carbon, and nitrogen elements considerably increases (titanium peak serves as the reference), and silicon element can be also observed. After the second functionalization step using F2, F3, or F4, the O1s/Ti2p and C1s/Ti2p ratios (Table S1, Supporting Information) are notably different from $Ti_3C_2T_x$-F1 suggesting further compositional rearrangements. The high-resolution Si2p spectra (Figure S3, Supporting Information) display the most intense peak is at 102.7 eV, which can be attributed to the Si–O–Si bond between neighboring F1 compounds due to condensation reaction, but also to the Si–O–Ti covalent bond formation between F1 and $Ti_3C_2T_x$.[62] This peak remains unaltered after the functionalization of $Ti_3C_2T_x$-F1 with F2, F3, or F4. The analysis of the high-resolution C1s spectra (Figure S4, Supporting Information) reveals an increase in the peak intensity at ≈286.5 eV from C–O chemical bond,[63] as well as the appearance of a new peak at 285.5 eV, corresponding to the C–N chemical bond.[64] At the same time, the high-resolution spectra of O1s (**Figure 2**) after functionalization reveal the significant increase in the intensity of the peaks at ≈532 and ≈533.4 eV due to the presence of additional chemical bonds at these regions, namely Si–O–Ti chemical bond, that confirms the formation of a covalent bond between compound F1 and $Ti_3C_2T_x$, as well as C–O chemical bond from F2, F3, and F4 organic compounds.[65] Moreover, a new peak at ≈532.7 eV is observed on the high-resolution O1s spectra corresponding to Si–O–Si chemical bond[66] that also confirms the condensation of compound F1. On the other hand, the high-resolution Ti2p spectrum (Figure S5, Supporting Information) remains unaltered after the two-step functionalization, suggesting no involvement of the titanium element in the $Ti_3C_2T_x$ functionalization.

The crystalline structures of pristine and functionalized $Ti_3C_2T_x$ are characterized by X-ray diffraction (XRD) (**Figure 3**a). $Ti_3C_2T_x$ exhibit an intense diffraction peak at $2\theta = 6.6°$, attributed to the 002 plane, which originates from the spacing between the layers (d = 1.34 nm, calculated using Bragg's law) as previously reported,[67–68] as well as other small diffraction peaks at 2θ = 19.7°, 26.5°, 33°, and 40°, respectively, attributed to the 004, 006, 008, and 104 basal planes. Upon functionalization of $Ti_3C_2T_x$ with F1, the peak attributed to the 002 plane is shifted toward lower angles, 2θ = 5.25°, which is connected with the

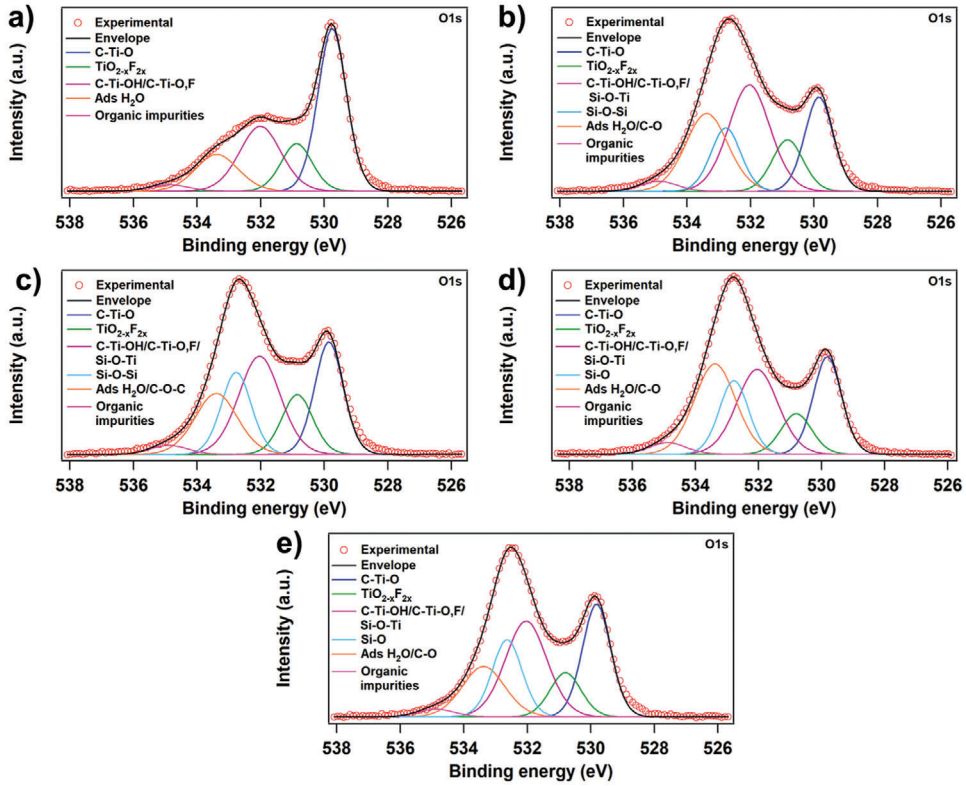

Figure 2. High-resolution O1s XPS spectra of: a) $Ti_3C_2T_x$, b) $Ti_3C_2T_x$-F1, c) $Ti_3C_2T_x$-F1+F2, d) $Ti_3C_2T_x$-F1+F3, and e) $Ti_3C_2T_x$-F1+F4.

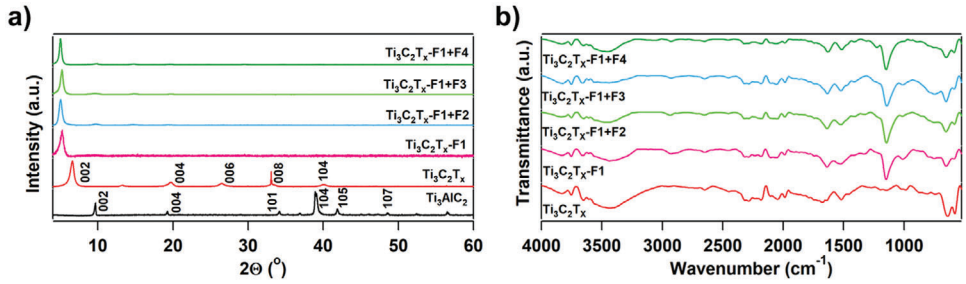

Figure 3. a) XRD diffractograms and b) FT-IR spectra of: Ti_3AlC_2, $Ti_3C_2T_x$, $Ti_3C_2T_x$-F1, $Ti_3C_2T_x$-F1+F2, $Ti_3C_2T_x$-F1+F3, and $Ti_3C_2T_x$-F1+F4.

$Ti_3C_2T_x$ interlayer distance increase (d = 1.68 nm). Accordingly, after the second functionalization step with the compounds F2, F3, and F4, the interlayer distance of $Ti_3C_2T_x$ is further increased to d≈1.75 nm in the three cases, which further indicates the successful functionalization of $Ti_3C_2T_x$-F1.

To gain additional information on the chemical composition of all $Ti_3C_2T_x$-based materials, Fourier transform infrared (FT-IR) analysis is performed (Figure 3b; and Figure S6, Supporting Information). In the starting material, $Ti_3C_2T_x$, the most pronounced peaks are located at 640 and 580 cm^{-1} and can be assigned to Ti–O and Ti–C out-of-plane vibrations (twisting or rocking), respectively (Figure S6a, Supporting Information).[69] Moreover, in $Ti_3C_2T_x$ spectrum, there is a peak centered at 1672 cm^{-1} that can be assigned to a stretching mode of C=O bond,[70] and the band around 3450 cm^{-1} can emerge from both –OH surface terminations and entrapped water molecules.[62]

The reduction of the intensity of the peaks corresponding to –OH, Ti–O, and Ti–C as well as the appearance of new peaks at ≈2900, at ≈1633 cm^{-1}, and between 1150–1000 cm^{-1} demonstrate the successful functionalization with F1. After the first functionalization step, two new peaks appear at 2939 and 2877 cm^{-1} that are attributed to symmetric and asymmetric vibrations of C–H bonds, respectively, in the alkyl chain of APTES.[62] At the same time, the presence of the new intense peak at 1149 cm^{-1} indicates the occurrence of Si–CH_2 band[71] as well as it can be assigned to the stretching mode of C–N bond[72] and Si–O–Si bond,[65] while the peak centered at 1012 cm^{-1} is attributed to a stretching Si–O–Ti bond.[65] The peak centered at 1672 cm^{-1} is shifted to 1633 cm^{-1}, which is attributed to a bending mode of N–H bond in amines as well as the peak centered at 1520 cm^{-1}. Importantly, the small peaks at 1750 and 1800 cm^{-1} can also be assigned to C=O bonds.[72]

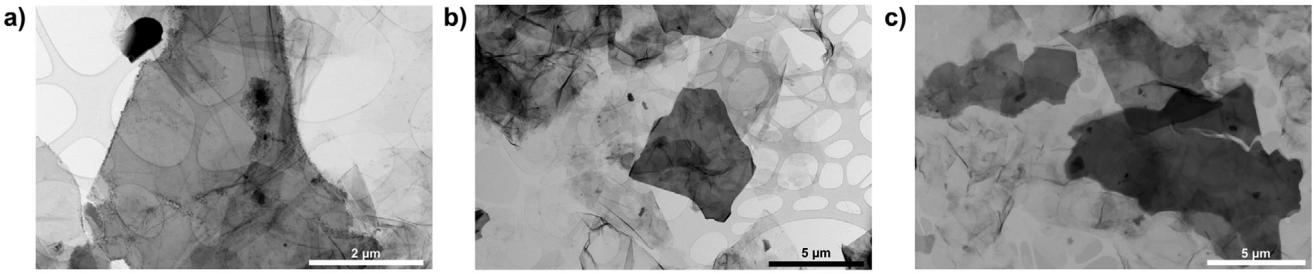

Figure 4. Representative STEM images of: a) $Ti_3C_2T_x$, b) $Ti_3C_2T_x$-F1, and c) $Ti_3C_2T_x$-F1+F3.

After the functionalization of $Ti_3C_2T_x$-F1 with F2, there is a small increase in the intensity of the peak at 1470 cm^{-1} that can be attributed to the increase in the amount of CH_2 groups. Moreover, the shoulder of the peak at ≈3450 cm^{-1} from the right side is shrunk, likely indicating the formation of secondary amine which has only one peak at ≈3300 cm^{-1}, while primary amines are characterized by two peaks, at ≈3400 and ≈3300 cm^{-1}, as in the case of $Ti_3C_2T_x$-F1. Furthermore, in $Ti_3C_2T_x$-F1+F3, a shoulder of the peak centered at 1149 cm^{-1} from the left side is more pronounced, while in $Ti_3C_2T_x$-F1+F4, a new peak is observed at 1225 cm^{-1} that can be assigned to the stretching mode of C–O band[73] confirming the presence of C–O–C and C–OH bonds in $Ti_3C_2T_x$-F1+F3 and $Ti_3C_2T_x$-F1+F4, respectively.

Scanning transmission electron microscopy (STEM) analysis is then performed to provide qualitative information on the morphology of $Ti_3C_2T_x$-based materials. According to the STEM images (**Figure 4**), pristine $Ti_3C_2T_x$ as well as materials obtained after the functionalization consist of ultrathin µm-sized flakes of irregular shapes. Upon functionalization, no clear changes in morphology are observed. Besides, no impurities are detected thanks to the thorough centrifugation steps both after the etching and exfoliation as well as after the subsequent functionalization steps.

2.2. Humidity Sensing Performance

Once the successful functionalization of $Ti_3C_2T_x$ is confirmed, pristine and functionalized $Ti_3C_2T_x$ films are deposited via dry transfer onto Si/SiO_2 substrates bearing eight pairs of interdigitated electrodes (IDEs) (Figure S7, Supporting Information). Scanning electron microscopy (SEM) reveals film thickness of ≈1–2 µm in all cases (Figure S8, Supporting Information). Three different devices of $Ti_3C_2T_x$ and $Ti_3C_2T_x$ -F1+F3 are fabricated to prove the reproducibility of the dry-transfer process (Figures S9 and S10, Supporting Information). As can be seen in Figures S9 and S10 (Supporting Information), in all cases the thin films are highly homogeneous and the thickness amounts to ≈1–2 µm. Moreover, the *I–V* curves of the 8 devices belonging to one substrate are presented in Figure S11 (Supporting Information). The average resistance of $Ti_3C_2T_x$ and $Ti_3C_2T_x$ -F1+F3 films amounts to 150.87 ± 17.69 and 359.41 ± 25.56 Ω, respectively. The RSD is below 10%, confirming the high reproducibility of the device fabrication process. The hydrophilicity of the different films is quantified by water contact angle (C.A.) measurements (Figures S12 and S13, Supporting Information) between 1 and 300 s. The average C.A. of $Ti_3C_2T_x$-based films gradually decreases in time, being $Ti_3C_2T_x$-F1+F3 always the most hydrophilic sample. In agreement with previous reports, the C.A. of $Ti_3C_2T_x$ is 61.5° ± 1.85°, which after F1 functionalization increases to 68.1° ± 0.68°. Among the three films prepared with $Ti_3C_2T_x$-F1 functionalized with F2-F4, $Ti_3C_2T_x$-F1+F2 films display the most hydrophobic profile (C.A. 90.9° ± 0.91°), then $Ti_3C_2T_x$-F1+F4 films are found to be more hydrophilic (C.A. 76.2° ± 0.76°) and $Ti_3C_2T_x$-F1+F3 results in being the most hydrophilic film (C.A. 53.7° ± 0.54°). We foresee that, although the use of F2-F4 molecules for the functionalization of $Ti_3C_2T_x$-F1 yields in the same interlayer spacing (i.e., d ≈1.75 nm), the major difference in hydrophobic/hydrophilic character will result in a very different response to moisture.

The first key performance indicator (KPI) to assess the humidity sensing performance is the sensitivity of the device. We determine the sensitivity of the different $Ti_3C_2T_x$-based films via direct current (DC) and alternating current (AC) measurements. For the DC measurements, *I–V* curves are obtained by applying a constant bias of 50 mV. First, the *I–V* curves of the bare substrate show an important hysteresis and minimal response to the RH level. Differently, the *I–V* curves of $Ti_3C_2T_x$-based devices (Figure S15, Supporting Information) reveal no hysteresis and an Ohmic behavior. From the *I–V* curves, the device's response can be calculated as $\Delta R/R_0$ (%), being R the device's resistance at a certain relative humidity (RH) level and R_0 the device's resistance at 0% RH. **Figure 5**a,b displays the device's response of the different $Ti_3C_2T_x$-based materials, as a function of the RH level. The response of all the pristine and functionalized $Ti_3C_2T_x$ devices vary linearly with the RH level and two different linear ranges are found, from 0% to 70% RH and from 70% to 100% RH. The sensitivity of each material is calculated from the slope of the linear fitting for both RH ranges (Figure S16, Supporting Information). As predicted from their highest hydrophilic character, the $Ti_3C_2T_x$-F1+F3 films exhibited the highest sensitivity in both RH ranges, being 0.777 and 3.035, respectively.

Additionally, electrochemical impedance spectroscopy (EIS), without applied bias, is also used to calculate the sensitivity of $Ti_3C_2T_x$-based films (Figure S17, Supporting Information). As can be seen in Figure S17 (Supporting Information), the Nyquist plots of $Ti_3C_2T_x$-based devices reveal a semicircle shape, whose diameter is dependent on the RH level. The electrical circuit model used for fitting the Nyquist plots can be seen in Figure S18a (Supporting Information). The charge transfer resistance of the $Ti_3C_2T_x$-based films is used to calculate the device's response and the sensitivity of each material in an analogous manner to the

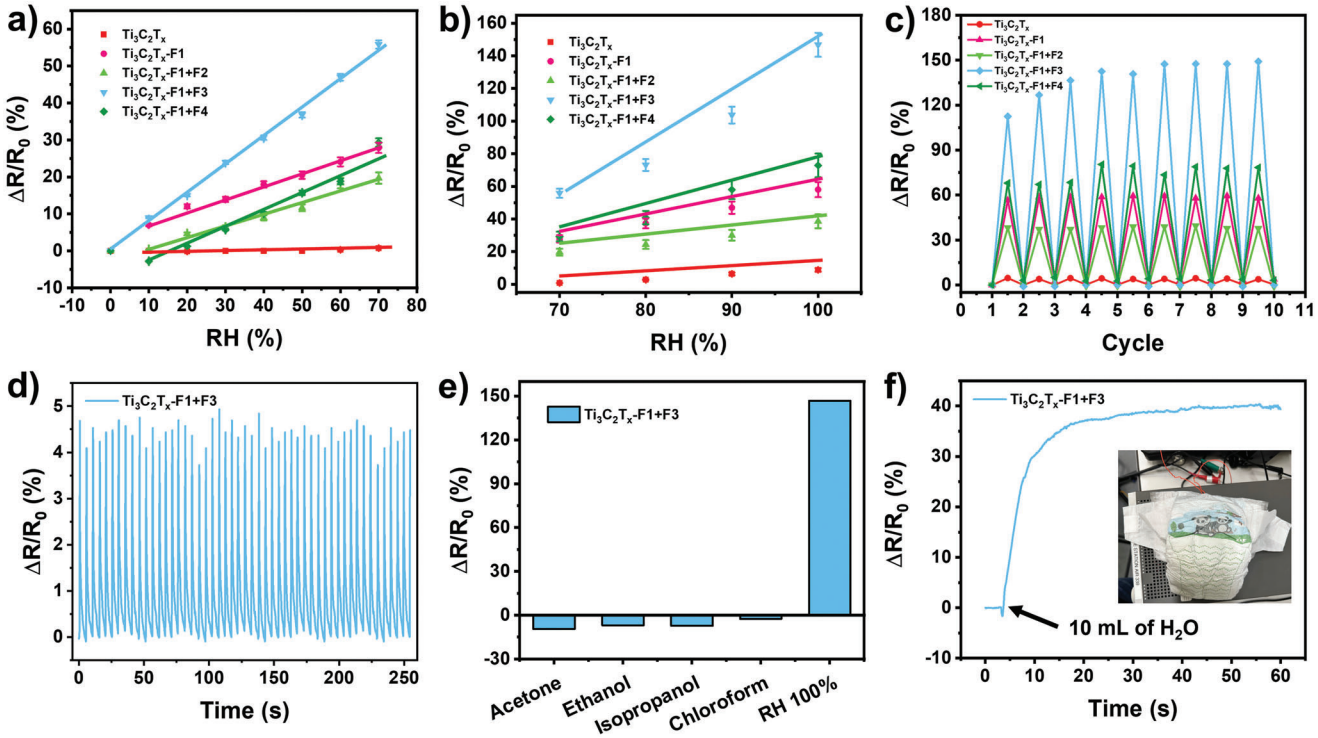

Figure 5. Humidity sensing performance of $Ti_3C_2T_x$-based devices. a–c) Response of $Ti_3C_2T_x$-based devices between a) 0–70% RH and b) 70–100% RH, and c) upon cycling between 0% and 100% RH for 10 times. d–f) Response of $Ti_3C_2T_x$-F1+F3 devices: d) when they are exposed to 50 cycles of humid air during the application of a constant bias of 50 mV, e) when they are exposed to saturated vapors of different interfering compounds, and f) for the real-time monitoring of an infant diaper's wetting.

DC measurements (Figure S18, Supporting Information). In full agreement with DC measurements, $Ti_3C_2T_x$-F1+F3 films exhibit the highest sensitivity, 1.218 and the same trend in sensitivity is obtained for the other $Ti_3C_2T_x$-based films.

Although in the present case we find a linear dependence of the sensor response with the RH level, some sensors do not exhibit a humidity response with a well-defined trend (e.g., linear, logarithmic, exponential). In those cases, the sensor sensitivity is usually defined as the maximum $\Delta R/R_0$ (%) achieved or simply as R/R_0. For a better comparison with state-of-the-art MXene-based humidity sensors, we calculate the sensitivity of $Ti_3C_2T_x$-based films using the three different methodologies (Table S3, Supporting Information). As can be seen in Table S3 (Supporting Information), if sensitivity is calculated using the R/R_0 approach, some of the capacitive MXene-based sensors as well as those where MXenes have been blended with polymers outperform $Ti_3C_2T_x$-F1+F3 films. However, the performance of those systems is not quantifiable as we discussed above. Importantly, if the sensitivity is calculated from the slope of the linear fitting or from $\Delta R/R_0$ (%), $Ti_3C_2T_x$-F1+F3 films exhibit a performance beyond the state of the art.

$Ti_3C_2T_x$-based devices are then cycled between 0% and 100% RH for 10 times to assess their reusability (Figure 5c; and Figure S19, Supporting Information). Figure 5c displays that all the devices retain a stable response between 0% and 100% RH even after 10 consecutive cycles. To prove the stability of our devices, the film resistance is monitored in time while applying a bias of 50 mV. As can be seen in Figure S20 (Supporting Information), the variation of resistance of all the devices is minimal after 140 s of continuous measurement.

Response and recovery time are then obtained by cycling the devices between low and high RH and plotting continuously the change in response over time (Figure S21, Supporting Information). For equitable comparison with state-of-the-art MXene-based humidity sensors, we use the "time per RH range tested" (having units of s RH^{-1}) introduced by An et al.,[51] as a figure of merit with the assumption that humidity response is linear (Table S3, Supporting Information). Significantly, $Ti_3C_2T_x$-F1+F3 devices respond in just 0.24 s RH^{-1} and fully recover in 0.40 s RH^{-1}. Conversely, the response time of $Ti_3C_2T_x$ sensor exhibits a twofold increase in the response but faster recovery (0.42 and 0.14 s RH^{-1}, respectively). The response and recovery time of the other three systems is comparable, $Ti_3C_2T_x$-F1 (0.37 and 0.49 s RH^{-1}, respectively), $Ti_3C_2T_x$-F1+F2 (0.35 and 0.49 s RH^{-1}, respectively) and $Ti_3C_2T_x$-F1+F4 (0.41 and 0.62 s RH^{-1}, respectively).

Figure 5d portrays the response of $Ti_3C_2T_x$-F1+F3 devices once exposed to a series of 50 humidity pulses. It shows that the response is almost constant for the $Ti_3C_2T_x$-F1+F3 device, even after 50 pulses and the small variations are more likely caused by the rough approach employed to provide the humid pulses. In addition, the response and recovery time for such short pulses are 500 ms and 2.5 s, respectively (Figure S22, Supporting Information), making $Ti_3C_2T_x$-F1+F3 devices compatible with real-time monitoring applications. To assess the long-term stability of $Ti_3C_2T_x$-F3 devices, two devices are stored under extreme conditions of humidity (i.e., one at 10% RH and other at 80% RH)

and their resistance is followed during 10 consecutive days (Figure S23, Supporting Information). As can be seen in Figure S23 (Supporting Information), the resistance of $Ti_3C_2T_x$-F3 sensors remains nearly constant (changes < 5%) for both humidity levels for 10 days, indicating the improved stability of pristine $Ti_3C_2T_x$ MXenes upon functionalization.

The selectivity of the $Ti_3C_2T_x$-F1+F3 devices in the presence of vapors of volatile organic compounds (VOCs) is also evaluated. In particular, the sensitivity toward ethanol, acetone, isopropanol, and chloroform is tested by recording the response of the devices in time, while exposing them subsequently to the equilibrium vapor pressure of the selected VOCs (Figure S24, Supporting Information). The maximum response achieved for each VOC can be seen in Figure 5e. It unambiguously shows that the response of $Ti_3C_2T_x$-F1+F3 to all of the VOCs is much lower (i.e., $\Delta R/R_0 = -9.45\%$ for acetone) than the response to moisture ($\Delta R/R_0 = 146.77\%$). The reusability of $Ti_3C_2T_x$-F1+F3 devices is also demonstrated as can be seen in Figure S24 (Supporting Information), where the device's initial response is fully recovered after their exposure to each VOC.

The effect of temperature on the resistance of pristine and functionalized $Ti_3C_2T_x$ films is also evaluated by keeping constant the humidity at 0% RH and varying the temperature from −23 to 67°C (Figure S25, Supporting Information). The resistance versus temperature plots display a metallic behavior for the systems with slightly different temperature coefficients (α) upon the Ti_3C_2T functionalization, ranging from 0.128 (pristine Ti_3C_2T) to 0.199 ($Ti_3C_2T_x$-F1+F3).

Benefiting from the superior performance of the $Ti_3C_2T_x$-F1+F3 devices, we explore its functional application as a humidity sensor in smart diapers. Intelligent or smart diapers represent a technology already available on the market that is gaining much attention as the sensor sends diaper change alerts to the caregiver instantly via an app, providing parents with peace of mind. As shown in Figure 5f, 10 mL water is used to simulate infant enuresis, the $Ti_3C_2T_x$-F1+F3 device attached to the diaper generates a spontaneous response as the ambient humidity increases, illustrating its compatibility with a practical application.

The changes in ΔR at different RH levels are commonly attributed to three different effects: i) electronic decoupling of individual MXene layers due to interlayer space increase (i.e., swelling mechanism), ii) charge depletion in the presence of adsorbed moisture (i.e., electron transport mechanism), and iii) water-induced chemical modification of the MXene surface (i.e., electron transport mechanism). Besides, depending on the organic molecule, other mechanisms, such as proton conduction can be found. However, for the proton conduction mechanism, a decrease in resistance is obtained when the RH level is increased and therefore is not the present case. To shed some light on the humidity sensing mechanism of $Ti_3C_2T_x$-based films, an in situ XRD characterization at different RH levels is performed (Figures S26 and S27, Supporting Information). The XRD spectrum of the empty chamber is included (Figure S26, Supporting Information) where two peaks are obtained at $2\theta = 44.2°$ and $2\theta = 51.5°$. The XRD spectra recorded in situ by systematically changing the RH provided information about the structure and the stability of $Ti_3C_2T_x$-based films under humidity exposure (Figure S27, Supporting Information). The variation of the interlayer distance with the RH level calculated from the XRD spectra using Bragg's law can be seen in Figure S28 (Supporting Information). In the three cases of $Ti_3C_2T_x$-F1+F2, $Ti_3C_2T_x$-F1+F3, and $Ti_3C_2T_x$-F1+F4, the negligible variation of the interlayer distance with the RH level (< 0.11 nm) are monitored, which is attributed to initial water intercalation. Furthermore, negligible changes in the crystallinity of the materials are observed upon exposure to high levels of RH, and the chemical modification of the MXene surface is also discarded. In the present case, the humidity sensing mechanism can be fully attributed to the charge depletion caused by the adsorbed moisture.

3. Conclusions

In summary, we performed the synthesis and functionalization of $Ti_3C_2T_x$ MXenes via an unprecedented two-reaction process. First, F1 was covalently linked to $Ti_3C_2T_x$ through a silylation reaction and then used as an anchoring point for the covalent post-functionalization $Ti_3C_2T_x$-F1 with various organic bromides (1-bromohexane, 1-bromo-2-(2-methoxyethoxy)ethane and 6-bromo-1-hexanol) via the formation of a C-N bond between the latter and F1.

Although the functionalization of $Ti_3C_2T_x$-F1 with F2, F3 and F4 resulted in the same interlayer distance, confirmed by XRD, their different hydrophilic/hydrophobic nature resulted in a very different sensitivity to moisture, being $Ti_3C_2T_x$-F1+F3 the most hydrophilic and sensitive system. As KPIs, $Ti_3C_2T_x$-F1+F3 devices can be used in a broad operation range (0-100% RH), high sensitivity, 0.777 (first linear range 0–70% RH) and 3.035 (second linear range 70–100% RH), fast response/recovery time (0.24 and 0.40 s ΔH^{-1}, respectively), high selectivity in the presence of other volatile organic compounds (e.g., acetone, ethanol, isopropanol or chloroform). Besides, a proof of concept humidity sensors compatible with smart diapers application was fabricated.

This study is of great importance as it presents a promising strategy for the covalent functionalization MXenes, paving the way towards their further functionalization with other organic compounds to improve and extend their properties for practical applications in (opto)electronic devices or other chemical sensors.

4. Experimental Section

Materials: Ti_3AlC_2 was purchased from (Carbon-Ukraine Ltd.). Hydrofluoric acid (HF) was purchased from Alfa Aesar, while hydrochloric acid was purchased from VWR. Lithium chloride (LiCl), (3-aminopropyl)triethoxysilane (APTES, F1), 1-bromohexane (F2), 1-bromo-2-(2-methoxyethoxy)ethane (F3), 6-bromo-1-hexanol (F4) and ethanol were purchased from Sigma Aldrich. All reagents were used as received.

Preparation of $Ti_3C_2T_x$: 5 g of Ti_3AlC_2 was gradually added to 50 mL acidic solution of hydrofluoric acid (27–29 M, 48–51 wt.%): deionized water: hydrochloric acid (12 M, 37 wt.%) with the ratio 1:3:6 v/v in a 125 mL propylene bottle at 0°C and stirred at 500 rpm for 60 min. Thereafter, the reaction mixture was stirred at 35°C for 24 h at 500 rpm. The etched multilayer MXene particles were washed by successive steps of centrifugation at relative centrifugal force (RCF) of 2493 g at 10 °C for 10 min and redispersion in deionized water, until the neutral pH was obtained. The collected MXene particles were added to 100 mL aqueous solution of 5% g/v lithium chloride and stirred at 25°C for 24 h at 500 rpm. The reaction mixture was then washed by successive steps of centrifugation (RCF of 2493 g

at 10 °C for 10 min) and redispersion of the precipitate in fresh deionized water until a very dark black supernatant, containing delaminated MXene flakes, was formed. From this point onward, after each centrifugation, the black supernatant was collected and combined. The procedure continued until the supernatant color turned semi-transparent dark green. The collected solution of delaminated MXene flakes was centrifuged at RCF 9420 g for 20 min. The transparent green supernatant was discarded and the collected precipitate was re-dispersed in 200 mL of fresh deionized water and shaken by a vortex mixer to form a uniform aqueous dispersion of delaminated MXene flakes with a concentration of 12.5 mg/mL, as measured by gravimetric vacuum filtration.

Preparation of $Ti_3C_2T_x$ Functionalized with Compound F1 – $Ti_3C_2T_x$-F1: Under a neutral atmosphere, 200 mg of $Ti_3C_2T_x$ with a concentration of 130 mg/mL was put in a Schlenck tube. After the addition of 6 mL of ethanol, 2 mL of Millipore water (18.2 MΩ•cm in 25°C) and 0.4 mL of F1, the dispersion was sonicated for 3 min and then stirred for 2 days at room temperature. Then, the obtained functionalized material was centrifugated at RCF 15 557 g for 15 min, 5 times in ethanol to remove the excess of F1. Each time, a new portion of ethanol was added to a precipitate (8 mL). The final functionalized material was kept in ethanol (1.5 mg/mL) under a neutral atmosphere at 4°C.

Preparation of $Ti_3C_2T_x$-F1 Functionalized with Compound F2, F3, or F4 – $Ti_3C_2T_x$-F1+F2, $Ti_3C_2T_x$-F1+F3, and $Ti_3C_2T_x$-F1+F4: Under neutral atmosphere, 8 mL of $Ti_3C_2T_x$ in ethanol with the concentration of 1.5 mg/mL was put in a Schlenck tube. Subsequently, 0.4 mL of compound F2, F3 or F4 was added to the dispersion and then stirred for 2 days at room temperature. Next, the obtained functionalized material was centrifugated at RCF 15 557 g for 15 min, 5 times in ethanol to remove the excess of compound F2, F3 or F4. The final functionalized material was kept in ethanol (1.5 mg/mL) under a neutral atmosphere at 4°C.

Substrate Fabrication: Bottom contact IDEs on Si/SiO_2 with 20 µm channel length were patterned by photolithography (AZ1505 photoresist and MIF726 developer, Micro Chemicals) using a Microtech LW405B laser writer. 5 nm Cr and 40 nm thick Au were thermally evaporated with Plassys MEB 300 following a lift-off process. Every chip contains 8 pairs of IDEs and a total number of 22 fingers. The electrodes' width and spacing were 20 µm.

Thin Films Fabrication: We deposited $Ti_3C_2T_x$-based films on the substrates via dry-transfer from a 0.45 µm polytetrafluoroethylene (PTFE) Omnipore™ membrane filter (Φ = 25 mm). After filtering 1 mL of $Ti_3C_2T_x$-based dispersion at 1.5 mg/mL, the filters were pressed against the substrates for 1 h, with a laboratory manual press. In order to prevent the contact of the pads with the $Ti_3C_2T_x$-based films, they were previously covered with blue tape. After the film transfer, the tape was peeled off gently (Figure S7).

Characterization Techniques: Zeta potential measurements of $Ti_3C_2T_x$, $Ti_3C_2T_x$-F1, $Ti_3C_2T_x$-F1+F2, $Ti_3C_2T_x$-F1+F3, and $Ti_3C_2T_x$-F1+F4 dispersions were recorded on Zetasizer Lab DLS instrument (Malvern Panalytical). X-ray photoelectron spectroscopy (XPS) analyses were carried out using a Thermo Scientific KAlpha X-ray photoelectron spectrometer with an aluminum X-ray source (energy 1.4866 keV) and working at pressure of 10^{-8}–10^{-9} mbar in the main chamber. The X-ray spot size was settled at 400 µm. Survey spectra were recorded as result of 20 scans with a pass energy of 200.00 eV and a step size of 1 eV, while high-resolution spectra were an average of 30 scans with a pass energy of 50.00 eV and a step size of 0.1 eV. The samples were prepared by attaching $Ti_3C_2T_x$, $Ti_3C_2T_x$-F1, $Ti_3C_2T_x$-F1+F2, $Ti_3C_2T_x$-F1+F3, and $Ti_3C_2T_x$-F1+F4 solids to a copper tape. Morphological characterization was performed using a scanning transmission electron microscope (STEM) with focused ion beam FEI Helios NanoLab 66. The samples were prepared by drop-casting of 60 µL of dilute solution of starting material and after functionalization on a lacey carbon copper grid, followed by solvent evaporation. Scanning electron microscopy (SEM) analysis was performed to determine the film thickness with a FEI Quanta 250 FEG instrument, operated in high vacuum mode (pressure in 10^{-4} Pa range) with accelerating voltages of 30 kV for the incident beam. The samples preparation for SEM analysis is described in thin films fabrication (above). The X-ray diffraction (XRD) measurements were carried out on a D8 Advanced Bruker diffractometer in the Bragg-Brentano geometry. The diffractometer was equipped with a front monochromator (Cu Kα1 wavelength λ = 0.154 056 nm) and a LynxEye_2 detector (1D mode). The X-ray beam was nickel-filtered to reduce the intensity of the Cu Kβ X-rays. XRD data were collected from 4° to 60° (2θ) with a step size of 0.01° at a scanning rate of 0.1 s/step. The sample was placed inside a Cryo & Humidity Chamber CHC plus+ Anton Paar mounted on the Bruker diffractometer. The atmosphere in the CHC plus+ Chamber is controlled by a CCU 100 combined Control Unit and a MHG-32 Modular Humidity Generator. Analysis was performed at 25°C in air with controlled relative humidity varying between 10 and 85%. The water contact angle (C.A.) measurements were performed with a Krüss DSA100S instrument by depositing on $Ti_3C_2T_x$-based films, sessile drops (2 µL) of water (5 different drops per sample). For each sample, the drop images at 1, 30, 60, 150, and 300 s were fitted by the Ellipse (Tangent-1) method and the mean values and standard deviation were reported.

Humidity Sensing Performance: The performance of humidity sensors has been investigated by direct current (DC) and alternating current (AC) electrical measurements. DC measurements were performed measuring the two-terminal device resistance at a constant bias of 50 mV. All DC electrical measurements were carried out in a probe station in ambient conditions by using a Keithley 2612B Source Meter unit (SMU). AC measurements were performed by means of Electrochemical Impedance Spectroscopy (EIS) employing a Metrohm Autolab PGSTAT204 potentiostat/galvanostat. The two-terminal EIS was recorded from 10^4 to 5×10^5 Hz, swept from high to low frequencies, with a sine-wave voltage signal amplitude of 50 mV (root-mean-square, RMS) and no applied bias.

Sensitivity: To measure the sensitivity, the devices were connected to the SMU or potentiostat in a closed chamber (Figure S14, Supporting Information). The RH level inside the chamber was controlled by filling it with dry nitrogen or humidity produced via a humidifier. The response of the devices was calibrated by reading the resistance and the corresponding RH values registered by two independent commercial hygrometers, while the level of humidity inside the chamber was increased from RH = 0% to 100% and vice versa.

Reusability and Stability: The stability over time and the cyclability of the devices were gauged alternating for 10 times the RH in the chamber between 0% and 100% and recording the resistance. Besides, the resistance of the devices was continuously monitored for 140 s while applying a constant bias of 50 mV.

Response and Recovery Time: The response of the devices was monitored in time while alternating the RH level from 0% to 100% RH and vice versa. The response and recovery times were calculated as the time interval between 0% and 100% RH and between 100 and 0% RH, respectively. The values of response and recovery time reported in the text are the arithmetic mean of five different pulses.

Humidity Pulses: To perform consecutive humidity pulses a glass stopcock connected to a balloon filled with humid air and fixed at 10 cm from the sample, was cyclically and manually opened.

Selectivity: The calibration of the sensitivity to different vapors (ethanol, acetone, isopropanol and chloroform) was performed inside a closed chamber at ambient RH (i.e., 40% RH). 200 µL of each analyte (ethanol 17.14 M, acetone 13.50 M, isopropanol 13.08 M, and chloroform 12.48 M) was deposited into the chamber and the chamber was immediately closed. We monitored changes in device response in real-time until the closed chamber was saturated with analyte vapors. When the response began to decline, we opened the chamber and continued to monitor the response until the initial response was recovered.

Temperature Calibration: The electrical devices were measured in a two-probe configuration in a customized Janis cryogenic probe station, connected to a semiconductor parameter analyzer (Keithley 4200A SCS). A Sumitomo RDK-408D2 cryogen-free closed cycle is thermally anchored to the copper sample holder and the temperature measurements are performed within the T range 340–250 K. The device current (I) is recorded by sweeping the voltage (V) from 50 to −50 mV. The resistance is calculated at the maximum voltage bias (50 mV) for the three systems.

Practical Application: For testing the humidity sensing performance in smart diapers a device was placed inside a diaper and the response was

monitored in time. After 5 s, 10 mL of water was added over the diaper emulating an infant diaper's wetting.

Supporting Information

Supporting Information is available from the Wiley Online Library or from the author.

Acknowledgements

The authors acknowledge funding from the Polish National Science Center (Grant Nos. 2018/29/N/ST5/00054 and 2019/35/B/ST5/01568), the European Commission through ERC project SUPRA2DMAT (No. GA-833707), the Graphene Flagship Core 3 project (No. GA-881603) as well as the Agence Nationale de la Recherche through the Interdisciplinary Thematic Institute SysChem via the IdEx Unistra (No. ANR-10-IDEX-0002) within the program Investissement d'Avenir, the Fondation Jean-Marie Lehn, the Institut Universitaire de France (IUF).

Conflict of Interest

The authors declare no conflict of interest.

Data Availability Statement

The data that support the findings of this study are available from the corresponding author upon reasonable request.

Keywords

covalent functionalization, humidity sensors, MXenes, $Ti_3C_2T_x$, water receptors

Received: December 13, 2022
Revised: January 27, 2023
Published online:

[1] A. Antonacci, F. Arduini, D. Moscone, G. Palleschi, V. Scognamiglio, *Trends Anal. Chem.* **2018**, *98*, 95.
[2] S. Mare, *J. Clean Prod.* **2015**, *88*, 297.
[3] S. Amendola, R. Lodato, S. Manzari, C. Occhiuzzi, G. Marrocco, *IEEE Internet Things J.* **2014**, *1*, 144.
[4] F. Bibi, C. Guillaume, N. Gontard, B. Sorli, *Trends Food Sci. Technol.* **2017**, *62*, 91.
[5] Z. Duan, Y. Jiang, H. Tai, *J. Mater. Chem. C* **2021**, *9*, 14963.
[6] T. A. Blank, L. P. Eksperiandova, K. N. Belikov, *Sens. Actuators, B* **2016**, *228*, 416.
[7] J. R. McGhee, J. S. Sagu, D. J. Southee, P. S. A. Evans, K. G. U. Wijayantha, *ACS Appl. Electron. Mater.* **2020**, *2*, 3593.
[8] B. Adhikari, S. Majumdar, *Prog. Polym. Sci.* **2004**, *29*, 699.
[9] E. Singh, M. Meyyappan, H. S. Nalwa, *ACS Appl. Mater. Interfaces* **2017**, *9*, 34544.
[10] M. S. Siddiqui, A. Mandal, H. Kalita, M. Aslam, *Sens. Actuators B* **2022**, *365*, 131930.
[11] D. H. Ho, Y. Y. Choi, S. B. Jo, J.-M. Myoung, J. H. Cho, *Adv. Mater.* **2021**, *33*, 2005846.
[12] W. Yuan, G. Shi, *J. Mater. Chem. A* **2013**, *1*, 10078.
[13] C. Anichini, W. Czepa, D. Pakulski, A. Aliprandi, A. Ciesielski, P. Samorì, *Chem. Soc. Rev.* **2018**, *47*, 4860.
[14] H.-L. Hou, C. Anichini, P. Samorì, A. Criado, M. Prato, *Adv. Funct. Mater.* **2022**, *32*, 2207065.
[15] S. Borini, R. White, D. Wei, M. Astley, S. Haque, E. Spigone, N. Harris, J. Kivioja, T. Ryhänen, *ACS Nano* **2013**, *7*, 11166.
[16] S. Some, Y. Xu, Y. Kim, Y. Yoon, H. Qin, A. Kulkarni, T. Kim, H. Lee, *Sci. Rep.* **2013**, *3*, 1868.
[17] G. Naik, S. Krishnaswamy, *Graphene* **2016**, *5*, 1.
[18] S. Gilje, S. Han, M. Wang, K. L. Wang, R. B. Kaner, *Nano Lett.* **2007**, *7*, 3394.
[19] M. Tang, C. Zhang, J.-Y. Zhang, Q.-L. Zhao, Z.-L. Hou, K.-T. Zhan, *Phys. Status Solidi A* **2020**, *217*, 1900869.
[20] T. Kuila, A. K. Mishra, P. Khanra, N. H. Kim, J. H. Lee, *Nanoscale* **2013**, *5*, 52.
[21] C. Anichini, A. Aliprandi, S. M. Gali, F. Liscio, V. Morandi, A. Minoia, D. Beljonne, A. Ciesielski, P. Samorì, *ACS Appl. Mater. Interfaces* **2020**, *12*, 44017.
[22] Y. Tai, T. K. Bera, G. Lubineau, Z. Yang, *J. Mater. Chem. C* **2017**, *5*, 3848.
[23] Y. Wei, P. Zhang, R. A. Soomro, Q. Zhu, B. Xu, *Adv. Mater.* **2021**, *33*, 2103148.
[24] C. Zhang, Y. Zhang, K. Cao, Z. Guo, Y. Han, W. Hu, Y. Wu, Y. She, Y. He, *Ceram. Int.* **2021**, *47*, 6463.
[25] A. M. Jastrzębska, B. Scheibe, A. Szuplewska, A. Rozmysłowska-Wojciechowska, M. Chudy, C. Aparicio, M. Scheibe, I. Janica, A. Ciesielski, M. Otyepka, M. W. Barsoum, *Mater. Sci. Eng. C* **2021**, *119*, 111431.
[26] J. Li, F. Zeng, J. K. El-Demellawi, Q. Lin, S. Xi, J. Wu, J. Tang, X. Zhang, X. Liu, S. Tu, *ACS Appl. Mater. Interfaces* **2022**, *14*, 45254.
[27] J. Zhou, X. Zha, F. Y. Chen, Q. Ye, P. Eklund, S. Du, Q. Huang, *Angew. Chem.* **2016**, *128*, 5092.
[28] H. Pazniak, A. S. Varezhnikov, D. A. Kolosov, I. A. Plugin, A. D. Vito, O. E. Glukhova, P. M. Sheverdyaeva, M. Spasova, I. Kaikov, E. A. Kolesnikov, P. Moras, A. M. Bainyashev, M. A. Solomatin, I. Kiselev, U. Wiedwald, V. V. Sysoev, *Adv. Mater.* **2021**, *33*, 2104878.
[29] B. Anasori, C. Shi, E. J. Moon, Y. Xie, C. A. Voigt, P. R. C. Kent, S. J. May, S. J. L. Billinge, M. W. Barsoum, Y. Gogotsi, *Nanoscale Horiz.* **2016**, *1*, 227.
[30] S. Sun, C. Liao, A. M. Hafez, H. Zhu, S. Wu, *J. Chem. Eng.* **2018**, *338*, 27.
[31] M. Hu, H. Zhang, T. Hu, B. Fan, X. Wang, Z. Li, *Chem. Soc. Rev.* **2020**, *49*, 6666.
[32] Q. Zhao, Q. Zhu, Y. Liu, B. Xu, *Adv. Funct. Mater.* **2021**, *31*, 2100457.
[33] J. Nan, X. Guo, J. Xiao, X. Li, W. Chen, W. Wu, H. Liu, Y. Wang, M. Wu, G. Wang, *Small* **2021**, *17*, 1902085.
[34] J. Zhu, E. Ha, G. Zhao, Y. Zhou, D. Huang, G. Yue, L. Hu, N. Sun, Y. Wang, L. Y. S. Lee, C. Xu, K.-Y. Wong, D. Astruc, P. Zhao, *Coord. Chem. Rev.* **2017**, *352*, 306.
[35] M. Zubair, M. M. Ul Hassan, M. T. Mehran, M. M. Baig, S. Hussain, F. Shahzad, *Int. J. Hydrogen Energy* **2022**, *47*, 2794.
[36] Y. Wei, R. A. Soomro, X. Xie, B. Xu, *J. Energy Chem.* **2021**, *55*, 244.
[37] Y. Yang, Y. Xu, Q. Li, Y. Zhang, H. Zhou, *J. Mater. Chem. A* **2022**, *10*, 19444.
[38] Y. Chen, C. Liu, S. Guo, T. Mu, L. Wei, Y. Lu, *Green Energy Environ.* **2022**, *7*, 394.
[39] M. Devaraj, S. Rajendran, T. K. A. Hoang, M. Soto-Moscoso, *Chemosphere* **2022**, *302*, 134933.
[40] C. Hu, X. Yu, Y. Li, J. Cheng, Q. Li, B. Xiao, *Appl. Surf. Sci.* **2022**, *592*, 153296.
[41] P. Abdul Rasheed, R. P. Pandey, T. Gomez, K. A. Jabbar, K. Prenger, M. Naguib, B. Aïssa, K. A. Mahmoud, *Electrochem. Commun.* **2020**, *119*, 106811.
[42] U. Amara, B. Sarfraz, K. Mahmood, M. T. Mehran, N. Muhammad, A. Hayat, M. H. Nawaz, *Microchim. Acta* **2022**, *189*, 64.

[43] D. Lei, N. Liu, T. Su, Q. Zhang, L. Wang, Z. Ren, Y. Gao, *Adv. Mater.* **2022**, *34*, 2110608.
[44] R. Bhardwaj, A. Hazra, *J. Mater. Chem. C* **2021**, *9*, 15735.
[45] E. S. Muckley, M. Naguib, H.-W. Wang, L. Vlcek, N. C. Osti, R. L. Sacci, X. Sang, R. R. Unocic, Y. Xie, M. Tyagi, E. Mamontov, K. L. Page, P. R. C. Kent, J. Nanda, I. N. Ivanov, *ACS Nano* **2017**, *11*, 11118.
[46] L.-X. Liu, W. Chen, H.-B. Zhang, Q.-W. Wang, F. Guan, Z.-Z. Yu, *Adv. Funct. Mater.* **2019**, *29*, 1905197.
[47] X. Guo, D. Kuang, Z. Zhu, Y. Ding, L. Ge, Z. Wu, B. Du, C. Liang, G. Meng, Y. He, *ACS Appl. Nano Mater.* **2021**, *4*, 11159.
[48] J. Wu, P. Lu, J. Dai, C. Zheng, T. Zhang, W. W. Yu, Y. Zhang, *Sens. Actuators B* **2021**, *326*, 128969.
[49] D. Wang, D. Zhang, P. Li, Z. Yang, Q. Mi, L. Yu, *Nanomicro Lett.* **2021**, *13*, 57.
[50] T. Li, T. Zhao, X. Tian, L. Yuan, X. Xue, Z. Wang, L. Yin, J. Zhang, *J. Mater. Chem. C* **2022**, *10*, 2281.
[51] H. An, T. Habib, S. Shah, H. Gao, A. Patel, I. Echols, X. Zhao, M. Radovic, M. J. Green, J. L. Lutkenhaus, *ACS Appl. Nano Mater.* **2019**, *2*, 948.
[52] Z. Wang, K. Yu, Y. Feng, R. Qi, J. Ren, Z. Zhu, *Appl. Surf. Sci.* **2019**, *496*, 143729.
[53] M.-y. Yang, M.-l. Huang, Y.-z. Li, Z.-s. Feng, Y. Huang, H.-j. Chen, Z.-q. Xu, H.-g. Liu, Y. Wang, *Sens. Actuators B* **2022**, *364*, 131867.
[54] Q. Zhao, Y. Jiang, Z. Duan, Z. Yuan, J. Zha, Z. Wu, Q. Huang, Z. Zhou, H. Li, F. He, Y. Su, C. Tan, H. Tai, *J. Chem. Eng.* **2022**, *438*, 135588.
[55] S. Huang, V. N. Mochalin, *Inorg. Chem.* **2019**, *58*, 1958.
[56] E. Lee, A. VahidMohammadi, B. C. Prorok, Y. S. Yoon, M. Beidaghi, D.-J. Kim, *ACS Appl. Mater. Interfaces* **2017**, *9*, 37184.
[57] W. Yuan, K. Yang, H. Peng, F. Li, F. Yin, *J. Mater. Chem. A* **2018**, *6*, 18116.
[58] H.-J. Koh, S. J. Kim, K. Maleski, S.-Y. Cho, Y.-J. Kim, C. W. Ahn, Y. Gogotsi, H.-T. Jung, *ACS Sens.* **2019**, *4*, 1365.
[59] M. Wu, M. He, Q. Hu, Q. Wu, G. Sun, L. Xie, Z. Zhang, Z. Zhu, A. Zhou, *ACS Sens.* **2019**, *4*, 2763.
[60] H. Jing, H. Yeo, B. Lyu, J. Ryou, S. Choi, J.-H. Park, B. H. Lee, Y.-H. Kim, S. Lee, *ACS Nano* **2021**, *15*, 1388.
[61] J. Ji, L. Zhao, Y. Shen, S. Liu, Y. Zhang, *FlatChem* **2019**, *17*, 100128.
[62] H. Riazi, M. Anayee, K. Hantanasirisakul, A. A. Shamsabadi, B. Anasori, Y. Gogotsi, M. Soroush, *Adv. Mater. Interfaces* **2020**, *7*, 1902008.
[63] V. Natu, M. Benchakar, C. Canaff, A. Habrioux, S. Célérier, M. W. Barsoum, *Matter* **2021**, *4*, 1224.
[64] M. Peng, M. Dong, W. Wei, H. Xu, C. Liu, C. Shen, *Carbon* **2021**, *179*, 400.
[65] A. Kong, Y. Sun, M. Peng, H. Gu, Y. Fu, J. Zhang, W. Li, *Colloids Surf. A* **2021**, *617*, 126388.
[66] Y. Zhang, L. Zhu, L. Chen, L. Liu, G. Ye, *Rev. Adv. Mater. Sci.* **2019**, *58*, 32.
[67] L. Zhang, W. Su, Y. Huang, H. Li, L. Fu, K. Song, X. Huang, J. Yu, C.-T. Lin, *Nanoscale Res. Lett.* **2018**, *13*, 343.
[68] X. Chen, Y. Zhu, M. Zhang, J. Sui, W. Peng, Y. Li, G. Zhang, F. Zhang, X. Fan, *ACS Nano* **2019**, *13*, 9449.
[69] M. Mahmood, A. Rasheed, I. Ayman, T. Rasheed, S. Munir, S. Ajmal, P. O. Agboola, M. F. Warsi, M. Shahid, *Energy Fuels* **2021**, *35*, 3469.
[70] S. Liu, F. Hu, W. Shao, W. Zhang, T. Zhang, C. Song, M. Yao, H. Huang, X. Jian, *Nanomicro Lett.* **2020**, *12*, 135.
[71] P. J. Launer, B. Arkles, in *Silicon Compounds: Silanes and Silicones*, (Eds: B. Arkles, G. L. Larson), Gelest Inc. , Morrisville, PA **2013**, p. 175.
[72] J. Coates, in *Encyclopedia of Analytical Chemistry* (Ed: R. A. Meyers), John Wiley & Sons Ltd., Chichester **2000**, p. 10815.
[73] R. M. Silverstein, F. X. Webster, D. J. Kiemle, *Spectroscopic Identification of Organic Compounds*, John Wiley & Sons, Inc., New York **2005**, p. 72.

